

Article

Improvement in Position Response of Laser Focus Controlled Magnetic Actuator Based on Mixed Sensitivity Robust Control

Liping Wu¹, Ling Tong^{1,*}, Guang Yang^{1,2}, Qi Zhang¹, Fangchao Xu¹, Junjie Jin¹, Xiaoyou Zhang^{1,3} and Feng Sun¹

¹ School of Mechanical Engineering, Shenyang University of Technology, Shenyang 110870, China

² School of Mechanical Engineering, Shenyang Aerospace University, Shenyang 110136, China

³ Department of Mechanical Engineering, Nippon Institute of Technology, Saitama 345-8501, Japan

* Correspondence: tongling@sut.edu.cn

Abstract: The relative position between the laser beam and the nozzle is controlled by laser-focus-controlled magnetic actuators to achieve non-coaxial laser cutting and improve laser cutting efficiency. In this paper, a 3-DOF (degrees of freedom) magnetic actuator is designed to solve the inconsistency of the laser beam focus and the nozzle focus in off-axis laser cutting. A mixed sensitivity robust controller is designed, and its simulation analysis and experimental research are carried out. First, the kinetic mathematical equations are established according to the structure of the actuator. Then, a mixed sensitivity robust controller is designed and analyzed using MATLAB/Simulink. The control performance is simulated and analyzed under 20% parameter variation and pulse disturbance with an uncertain mathematical model and external disturbance, respectively. Finally, the experimental study of the step response of the actuator is carried out. The experimental results show that the step response of the actuator in the Y, X, and θ directions can quickly reach the steady-state value. Furthermore, the steady-state error in the X is 1.6%; the steady-state error in the Y is 0.39%; the steady-state error in the θ is 0.45%. Their errors are all less than 0.025 mm, so they meet the position performance requirements. It can provide technical support for laser off-axis cutting.

Keywords: electromagnetic drive; mixed sensitivity; robust control; differential control



Citation: Wu, L.; Tong, L.; Yang, G.; Zhang, Q.; Xu, F.; Jin, J.; Zhang, X.; Sun, F. Improvement in Position Response of Laser Focus Controlled Magnetic Actuator Based on Mixed Sensitivity Robust Control. *Actuators* **2023**, *12*, 4. <https://doi.org/10.3390/act12010004>

Academic Editor: Kirill Poletkin

Received: 5 November 2022

Revised: 6 December 2022

Accepted: 19 December 2022

Published: 21 December 2022



Copyright: © 2022 by the authors. Licensee MDPI, Basel, Switzerland. This article is an open access article distributed under the terms and conditions of the Creative Commons Attribution (CC BY) license (<https://creativecommons.org/licenses/by/4.0/>).

1. Introduction

Laser cutting has become the most widely used cutting technology [1–3] in the current manufacturing industry due to its characteristics such as no contact with the workpiece during processing [4,5], concentrated energy, low contamination of the workpiece, easy guidance, and easy automation control. The manufacturing industry places higher demands on machining accuracy and processing efficiency. Traditional laser cutting technology cannot meet the required cutting quality and efficiency. Therefore, improving laser cutting quality [6,7] and cutting efficiency [8] has become one of the hot spots of research and concern for scholars in related fields [9,10]. Elsheikh A. et al. conducted cutting experiments on CO₂ laser cutting of PMMA sheets, analyzed the factors affecting the kerf geometry, and used a genetic algorithm to select the optimal cutting parameters. The results showed that this method could significantly improve kerf quality [11]. Vora J. et al. analyzed the influence of different laser cutting process parameters on the incision quality. The results showed that the gas pressure had the greatest influence on the cutting quality [12]. Hong L. et al. studied the laser cutting of silicon steel sheets. They verified the operation of rotating airflow laser cutting by adding a cyclone deslagger at the bottom of the cut workpiece [13]. Quintero F. et al. designed a cutting experiment that was performed by changing the angle between the laser lens axis and the auxiliary gas axis. The results showed that the quality and efficiency of the cut could be improved [14,15]. The laser cutting head and the auxiliary gas of variable angle laser cutting are separated, so the cutting quality and efficiency differ

in each feeding direction. At the same time, there is no gas pressure at the laser beam, which may cause slag splashing and contamination of the lens, seriously affecting the cutting quality and efficiency. The problem of variable angle cutting can be solved by non-coaxial cutting of the laser beam and the gas flow beam. The principle of this cutting method is to separate the laser cutting head's auxiliary gas from the laser beam's central axis for laser cutting. Riveiro A. et al. conducted an experimental study of cutting aluminum alloys using an off-axis supersonic nozzle, analyzed the effect of machining parameters on cutting speed and cutting quality, and obtained the best results at high-frequency pulses [16]. They also developed an off-axis supersonic rectangular nozzle. They compared it with a coaxial nozzle, and the results showed that the newly designed off-axis supersonic rectangular nozzle gas injection system significantly improved cutting quality and efficiency [17]. Yagi A. et al. investigated the effect of off-axis position on laser cutting quality in nitrogen-assisted gas fiber laser cutting. Laser cutting was studied by varying the relative positions of the laser beam's central axis and the nozzle's central axis. The experimental results showed that the nozzle shifting setup could over obtain a comparable dross height for the coaxial setup and reduce the consumption of auxiliary gas [18]. These studies can effectively improve the quality of laser cutting. Based on the above literature review, it is necessary to design a high-speed, high-precision, interference-resistant, and compact actuator to control the position of the laser lens for automatic non-coaxial laser cutting.

Conventional mechanical actuators are characterized by complex mechanical structures between components, the need for lubrication, slow response speed, and low positioning accuracy [19]. Therefore, they cannot meet the high speed, precision, and compact structure standards required. Electromagnetic drive technology has the characteristics of a simple structure, compact structure, and no need for lubrication [20–26], which can meet the needs of non-coaxial laser cutting actuators. Zhang X. et al. designed a high-speed, high-precision electromagnetic actuator that can be connected with traditional laser cutting machine tools to control the relative position of the laser beam's axis and the auxiliary gas's axis [27]. He D. et al. proposed a 6-DOF (degrees of freedom) magnetically levitated lens-driven actuator for off-axis laser cutting control [28,29]. M Y. et al. investigated a 2-DOF electromagnetic actuator for laser off-axis cutting and achieved a positioning stroke of $\pm 500 \mu\text{m}$ [30]. In the magnetic drive system, there are some unmodeled parts and uncertain disturbances, and robust control can stabilize the control under model uncertainty [31,32]. Due to the characteristics of robust control, there have been many studies in the past decades, among which hybrid sensitivity robust control is the commonly used method [33–36]. However, most of the existing research on magnetically driven actuators was carried out on the basis of actuator model determination. The electromagnetic actuator is subject to strong nonlinearity and uncertainty disturbances. Considering the exact model of nonlinearity will increase the difficulty of controller design.

In summary, this paper takes the LCY-YAG laser cutting machine, a Beijing Zhengtian Hengye Numerical Control Technology Co., LTD. product, as the object and designs a 3-DOF actuator with electromagnetic drive and permanent magnet self-reset. The actuator uses three groups of differentially arranged electromagnets to provide driving force, a pair of axially placed and axially magnetized permanent magnets to provide recovery force, and the position of the actuator is detected by the eddy current displacement sensor. There are some parameters of the actuator that cannot be accurately modeled. The mixed sensitivity robust control strategy is selected to control the system stably. By choosing the weighting function, the controller model is obtained [37–40], and the position response simulation and experiment of the actuator are carried out. The actuator structure is simple and reliable. Experimental results show that the actuator can achieve position response and trajectory centering in the xOy plane and has anti-interference characteristics. The steady-state error is 0.016 mm, which meets the design requirement of the laser cutting machine's precision of 0.025 mm. The novelty of this paper is the design of a 3-DOF electromagnetic actuator for off-axis laser cutting applications. The self-resetting module of the actuator adopts a single magnetic spring structure, which solves the deviation of the position of the electromagnetic

actuator caused by inaccurate processing or installation caused by the self-resetting module composed of three magnetic springs designed in the literature [41].

This paper consists of six sections. In Section 2, the structure and mathematical model of the actuator are presented. The design of the hybrid sensitivity robust controller is given in Section 3. In Section 4, the simulation analysis is performed. Experimental verification is carried out in Section 5. Conclusions are given in Section 6.

2. Structural and Mathematical Models

2.1. Structure of the Actuator

The purpose of the actuator is to drive the position of the laser lens to achieve off-axis laser cutting. The actuator mainly consists of a drive module, a self-resetting module, a support module, and a detection module, as shown in Figure 1. The driving part consists of three pairs of differential electromagnets (EM), permalloy, frame, and moving plate. The self-resetting part consists of two ring-shaped permanent magnets (PM) of the same size, axially magnetized and axially mounted in parallel. One ring-shaped permanent magnet is fixed to the frame, and the other is fixed to the moving plate. The support component consists of a ceramic thrust ball bearing, the frame, and the moving plate. The detection component consists of an eddy current sensor and a position detection block.

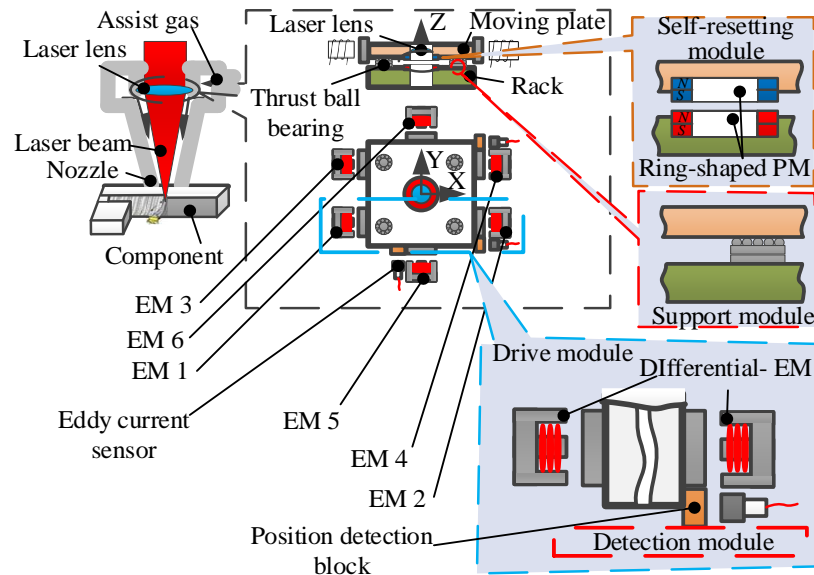


Figure 1. Actuator structure. The mechanical structure of the actuator is shown.

2.2. The Principle of the Actuator

The actuator can translate in the X and Y directions and rotate around the Z axis. The actuator principle relies on a differential electromagnet to provide the driving force, which makes the moving plate move, as shown in Figure 2. The recovery force and initial stiffness are provided by two axially magnetized permanent magnets. The position real-time feedback signal is provided by an eddy current displacement sensor. The motion in the X direction is driven by two pairs of differential electromagnets consisting of electromagnets 1 and 2 and electromagnets 3 and 4. The motion in the Y direction is driven by a pair of differential electromagnets consisting of electromagnets 5 and 6. The rotation motion around the Z axis is acted by three pairs of differential electromagnets.

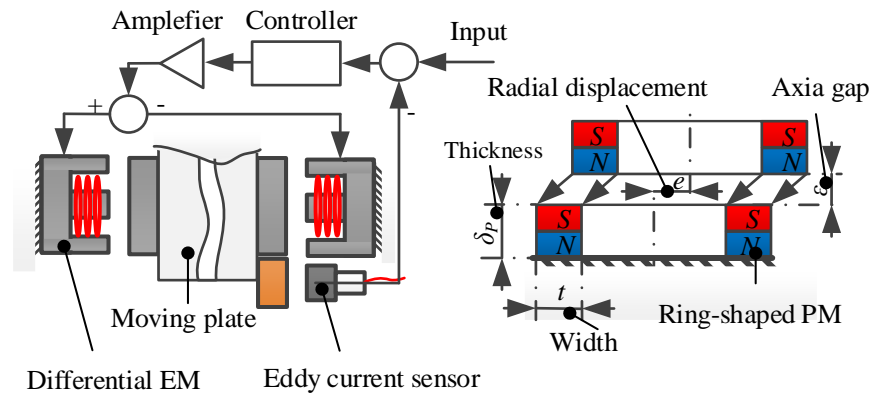


Figure 2. Working principle of the actuator.

2.3. The Mathematical Model of the Actuator

The force analysis of the actuator is shown in Figure 3. According to the structure of the actuator, when taking the equilibrium position, the center of mass O of the moving plate is the origin of the coordinates, and its coordinates are represented by (x, y, θ) . The X and Y are pointing, and counterclockwise rotation around the Z axis is shown in Figure 3 as the positive direction. When an input signal is given to the actuator, the actuator moves the moving plate, and the signals detected by the sensor are $x_1, x_2,$ and y_1 ; the driving forces provided by the three pairs of differential electromagnets are $F_{x1}, F_{x2},$ and F_{y1} ; the ring-shaped permanent magnet The provided restoring force is F_e (which can be decomposed into F_{ex} and F_{ey}); frictional resistance f_x, f_y ; frictional resistance torque M_θ . Under the action of these resultant forces (or resultant torque), the moving plate moves to a new equilibrium position O' (x_1, x_2, y_1). N_c is the detection point of sensor 1; M_c is the detection point of sensor 2; P_c is the detection point of sensor 3; N is the action point of the differential electromagnet force composed of electromagnet 3 and electromagnet 4; M is the action point of the differential electromagnet force composed of electromagnet 1 and electromagnet 2; P is the action point of the differential electromagnet force composed of electromagnet 5 and electromagnet 6.

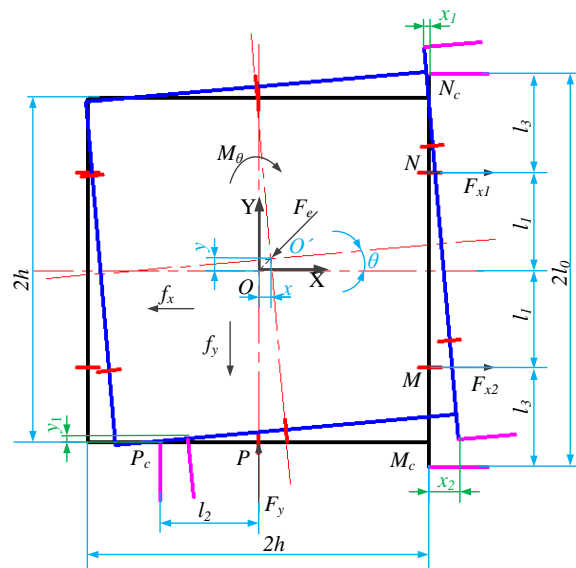


Figure 3. Force analysis diagram.

According to the force analysis, the movement of the center of mass of the moving plate of the actuator is $X, Y,$ and θ , and the signals detected by the sensor are $x_1, x_2,$ and

y_1 . To facilitate modeling, the coordinate system is transformed. It can be known from the geometric relationship:

$$\begin{cases} x = [(x_1 + \varepsilon x_1) + (x_2 + \varepsilon x_2)]/2 \\ y = y_1 + \varepsilon y_1 \\ \theta \approx \tan\theta = (x_2 - x_1)/2l_0 \end{cases} \quad (1)$$

where εx_1 , εx_2 , and εy_1 are the influence of the rotation angle θ on the detected values x_1 , x_2 , and y_1 .

It can be known from the geometric relationship (as shown in Figure 4).

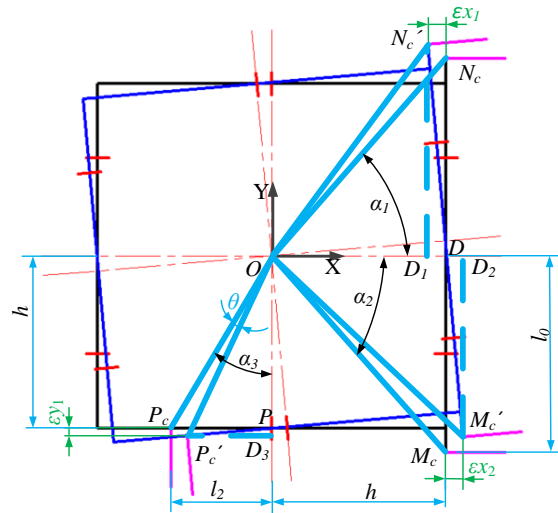


Figure 4. Analysis of the influence of the rotation angle on the detection position.

In $Rt\Delta ODNC$ and $Rt\Delta OD_1NC'$,

$$|\varepsilon x_1| = (l_0/\sin \alpha_1) \cdot [\cos \angle(\alpha_1 + \theta) - \cos \angle\alpha_1] \quad (2)$$

In $Rt\Delta ODMC$ and $Rt\Delta OD_2MC'$, the geometric relationship:

$$|\varepsilon x_2| = (l_0/\sin \alpha_2) \cdot [\cos \angle(\alpha_2 - \theta) - \cos \angle\alpha_2] \quad (3)$$

In $Rt\Delta OPPC$ and $Rt\Delta OD_3PC'$,

$$|\varepsilon y_1| = (l_2/\sin \alpha_3) \cdot [\cos \angle(\alpha_3 - \theta) - \cos \angle\alpha_3] \quad (4)$$

The detection position in the x direction is symmetrical, so $\alpha_1 = \alpha_2$. After arranging Formulas (2)–(4) and bringing them into Formula (1), we obtain:

$$\begin{cases} x = (x_1 + x_2)/2 + h \cdot (\cos \theta - 1) \\ y = y_1 + h \cdot (\cos \theta - 1) + l_2 \sin \theta \\ \theta \approx \tan\theta = (x_2 - x_1)/(2l_0) \end{cases} \quad (5)$$

The value of θ is extremely small, so if $\cos \theta$ approaches one and $\sin \theta$ approaches zero, then Formula (5) can be simplified as:

$$\begin{cases} x = (x_1 + x_2)/2 \\ y = y_1 \\ \theta = (x_2 - x_1)/(2l_0) \end{cases} \quad (6)$$

The dynamic equation of the actuator is:

$$\begin{cases} m\ddot{x} = F_{x1} + F_{x2} - F_{ex} - f_x \\ m\ddot{y} = F_y - F_{ey} - f_y \\ J\ddot{\theta} = -F_{x1} \cdot l_1 + F_{x2} \cdot l_1 - M_\theta \end{cases} \quad (7)$$

where m is mass of moving plate, J is the moment of inertia of the moving plate around the Z axis; x is the displacement of the moving plate along the X direction; y is the displacement of the moving plate along the Y direction; θ is the angle that the moving plate rotates around the Z axis; F_{x1} is the resultant force of the differential electromagnet composed of electromagnet 3 and electromagnet 4; F_{x2} is the resultant force of the differential electromagnet composed of electromagnet 1 and electromagnet 2; F_y is the resultant force of the differential electromagnet composed of electromagnet 5 and electromagnet 6; F_{ex} is the component force of the restoring force F_e generated by the annular permanent magnet in the X direction; F_{ey} is the component force of the restoring force F_e generated by the annular permanent magnet in the y direction; f_x is the friction force generated in the X direction; f_y is the friction force generated in the Y direction; M_θ is the frictional resistance torque generated around the Z axis; l_1 is the distance from the action point of F_{x1} to the central axis.

The electromagnet is a nonlinear element arranged differentially and can be linearized near the operating point. The force of the differential electromagnet is:

$$F_\lambda = \frac{4\mu_0 N^2 A}{(2\delta)^2} \cdot \frac{i_0^2}{d_0^3} \cdot \lambda + \frac{4\mu_0 N^2 A}{(2\delta)^2} \cdot \frac{i_0}{d_0^2} \cdot i_\lambda; (\lambda = \Delta x_1; \Delta x_2; \Delta y) \quad (8)$$

where μ_0 is magnetic permeability; N is the number of turns of the electromagnet coil; A is the cross-sectional area of the magnetic circuit in the E-type iron core; δ is the magnetic circuit reluctance coefficient; i_0 is the bias current of the electromagnet coil; d_0 is the initial air gap between the electromagnet and the armature; λ is the displacement change detected by the sensor; i_λ is control current.

Displacement stiffness coefficient k_x and the current stiffness coefficient k_i is introduced. Formula (8) is simplified as:

$$\begin{aligned} F_\lambda &= k_x \cdot \lambda + k_i \cdot i_\lambda; (\lambda = \Delta x_1, \Delta x_2, \Delta y) \\ k_x &= 4 \cdot \frac{\mu_0 N^2 A}{(2\delta)^2} \cdot \frac{i_0^2}{d_0^3}; k_i = 4 \cdot \frac{\mu_0 N^2 A}{(2\delta)^2} \cdot \frac{i_0}{d_0^2}; \end{aligned} \quad (9)$$

λ is positive in the direction away from the sensor, so it is a unified force system coordinate system and a generalized coordinate system.

Therefore, $\Delta x_1 = -x_1$, $\Delta x_2 = -x_2$, $\Delta y = y$.

According to Kirchhoff's law and the virtual displacement method, the restoring force of the annular permanent magnet is solved, and the restoring force F_e is obtained as [42]. The F_e can be found in Appendix A.

F_e is nonlinear. The k_e of Formula (10) can be found in Appendix A. In order to reduce the complexity of the control system, Taylor series expansion is performed at $e_0 = 0$, and the high-order infinitesimal quantities are omitted to obtain:

$$F_e = k_e \cdot e \quad (10)$$

where k_e is the restoring force coefficient of the ring permanent magnet.

Formulas (6), (9) and (10) are brought into Formula (7) to solve the dynamic equation.

$$\begin{cases} m\ddot{x} = -(2k_x + k_e)x + k_i(i_{x1} + i_{x2}) - c\dot{x} \\ m\ddot{y} = (k_x - k_e)y + k_i i_{y1} - c\dot{y} \\ J\ddot{\theta} = -2l_0 l_1 k_x \theta + l_1 k_i (i_{x2} - i_{x1}) - c_\theta \dot{\theta} \end{cases} \quad (11)$$

The Laplace transform of Formula (11) is:

$$\begin{cases} X(s) = \frac{k_i}{ms^2+cs+(2k_x+k_e)} [I_{x1}(s) + I_{x2}(s)] \\ Y(s) = \frac{k_i}{ms^2+cs+(k_e-k_x)} I_y(s) \\ \theta(s) = \frac{l_1k_i}{Js^2+c_\theta s+2l_0l_1k_x} [I_{x2}(s) - I_{x1}(s)] \end{cases} \quad (12)$$

3. Mixed Sensitivity Robust Controller Design

According to Formulas (6), (9) and (10), it can be seen that the measurement value of the sensor ignores the influence of the rotation angle and the driving force, and the restoring force ignores the high-order term of the Taylor expansion. The actuator has external environmental interference and some inevitable modeling errors. A mixed sensitivity robust control strategy is adopted to ensure the system can work stably under the above uncertain conditions. The system control block diagram is shown in Figure 5.

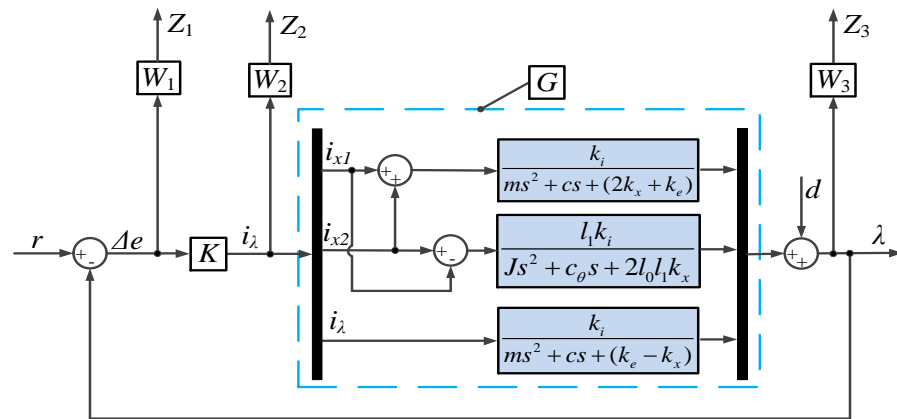


Figure 5. System control diagram. The control block diagram of the system is shown.

G is the system open-loop transfer function; K is the controller; Δe is position error; r is reference input; i_λ is control current; λ is system output; d is the system interference signal; W_1 is performance weight function; W_2 is control function; W_3 is robust weight function; $Z_1, Z_2,$ and Z_3 are evaluation system output.

The closed-loop transfer functions from r to $\Delta e, i_\lambda,$ and λ are:

$$\begin{cases} S = \frac{\Delta E(s)}{R(s)} = \frac{I}{I+GK} \\ R = \frac{I_\lambda(s)}{R(s)} = \frac{K}{I+GK} = KS \\ T = \frac{\lambda(s)}{R(s)} = \frac{GK}{I+GK} = I - S \end{cases} \quad (13)$$

where S is the system sensitivity function, and T is the system-supplemented sensitivity function.

The purpose of designing the mixed sensitivity H_∞ controller is to reasonably select $W_1, W_2,$ and $W_3,$ so that Formula (14) meets the requirements.

$$\|W_1S \quad W_2R \quad W_3T\|_\infty^T = \gamma \leq 1 \quad (14)$$

In general, in electromagnetic drive systems, external disturbances are at low frequencies, and unmodeled disturbances are at high frequencies. Therefore, in selecting the weighting function, W_1 and W_3 should have low-pass and high-pass filtering properties, respectively.

To avoid increasing the actuator order, W_2 usually takes a constant value. According to the above analysis, W_1 , W_2 , and W_3 are selected as:

$$\begin{cases} W_1(s) = k_1/(1 + \tau_1 s) \\ W_2(s) = k_2 \\ W_3(s) = k_3 s(1 + \tau_3 s) \end{cases} \quad (15)$$

where k_1 , k_2 , k_3 , τ_1 , and τ_3 are the coefficients of the weighting function, respectively.

The values in Table 1 are brought into Formula (10) to calculate k_e , and the results are shown in Table 2.

Table 1. Parameters of ring permanent magnets.

System Parameters	Symbol	Value
Air permeability	μ_0 (H/m)	$4\pi \times 10^{-7}$
Relative permeability	μ_r	1.05
Material remanence	B_r (T)	1.18
Number of permanent magnets	n	2
Permanent magnet thickness	δ_P (mm)	4
Permanent magnet inner diameter	r_1 (mm)	15
Permanent magnet outer diameter	r_2 (mm)	20.5
Permanent magnet axial air gap	ε (mm)	4
Permanent magnet radial displacement	e (mm)	$0 < e < 4$

Table 2. Parameters of system.

System Parameters	Symbol	Value
Moving plate weight	m (kg)	1.3995
The distance between two pairs of electromagnet force centers in the X direction	l_1 (mm)	44.5
The X direction sensor measures the distance from the point to the center	l_0 (mm)	167
The rotational inertia of the moving plate	J (kg·mm ²)	0.004972
The magnetic permeability of air	μ_0 (H/m)	$4\pi \times 10^{-7}$
Number of coil turns	N	128
The cross-sectional area of the magnetic circuit	S (mm ²)	912
Magnetic circuit reluctance coefficient	δ	1.38
X direction damping	c_x	10
Y direction damping	c_y	10
θ direction damping	c_θ	10
Initial current	i_0 (A)	1.2
Initial gap	d_0 (mm)	2
Permanent magnet stiffness	k_e (N/m)	3032.7

The mixing sensitivity controller K is solved by selecting the appropriate coefficients.

The parameters in Table 2 are brought into Formula (12) to obtain the transfer function of the system as:

$$\begin{cases} G_x(s) = \frac{2.96}{1.3995s^2 + 10s + 6582.1} \\ G_y(s) = \frac{2.96}{1.3995s^2 + 10s + 1258} \\ G_\theta(s) = \frac{0.13}{0.00497s^2 + 10s + 13.19} \end{cases} \quad (16)$$

The Y direction parameters are selected as $k_1 = 1500$, $k_2 = 0.002$, $k_3 = 0.01$, $\tau_1 = 100$, $\tau_3 = 0.01$, and the calculated $\gamma = 0.9338$. The controller is:

$$G_y(s) = \frac{6.0557e05(s^2 + 7.145s + 898.9)}{(s + 0.01)(s^2 + 1328.37s + 33057.11)} \quad (17)$$

The X direction parameters are selected as $k_1 = 1500$, $k_2 = 0.0004$, $k_3 = 0.01$, $\tau_1 = 100$, $\tau_3 = 0.01$, and the calculated $\gamma = 0.9186$. The controller is:

$$G_x(s) = \frac{1.7905e06(s^2 + 7.145s + 898.9)}{(s + 876.5)(s + 66.32)(s + 0.01)} \quad (18)$$

The θ direction parameters are selected as $k_1 = 2000$, $k_2 = 0.0004$, $k_3 = 0.01$, $\tau_1 = 100$, $\tau_3 = 0.01$, and the calculated $\gamma = 0.8411$. The controller is:

$$G_\theta(s) = \frac{6.6604e05(s^2 + 2012.32s + 2654.52)}{(s + 2090)(s + 350.2)(s + 0.01)} \quad (19)$$

4. Simulation Analysis

4.1. Analysis of the Performance of the Control System

4.1.1. Analysis of the Performance of the Y Direction Control System

The amplitude-frequency characteristic curves of $S(s)$ and $W_1^{-1}(s)$ in the Y direction are shown in Figure 6a. The amplitude of $\bar{\sigma}(S(s))$ is extremely small in the low-frequency range, and its maximum amplitude is less than $\bar{\sigma}(W_1^{-1}(s))$ in the whole frequency range, which satisfies Formula (20). Therefore, the anti-interference ability and tracking characteristics of the system are ensured. The amplitude-frequency characteristic curves of $T(s)$ and $W_3^{-1}(s)$ are shown in Figure 6b. $\bar{\sigma}(T(s))$ has a large slope in the high-frequency range, and its maximum amplitude is smaller than $\bar{\sigma}(W_3^{-1}(s))$ in the whole frequency range, which satisfies Formula (21). It ensures that high-frequency noise is rapidly attenuated.

$$\bar{\sigma}(S(s)) \leq \bar{\sigma}(W_1^{-1}(s)) \quad (20)$$

$$\bar{\sigma}(T(s)) \leq \bar{\sigma}(W_3^{-1}(s)) \quad (21)$$

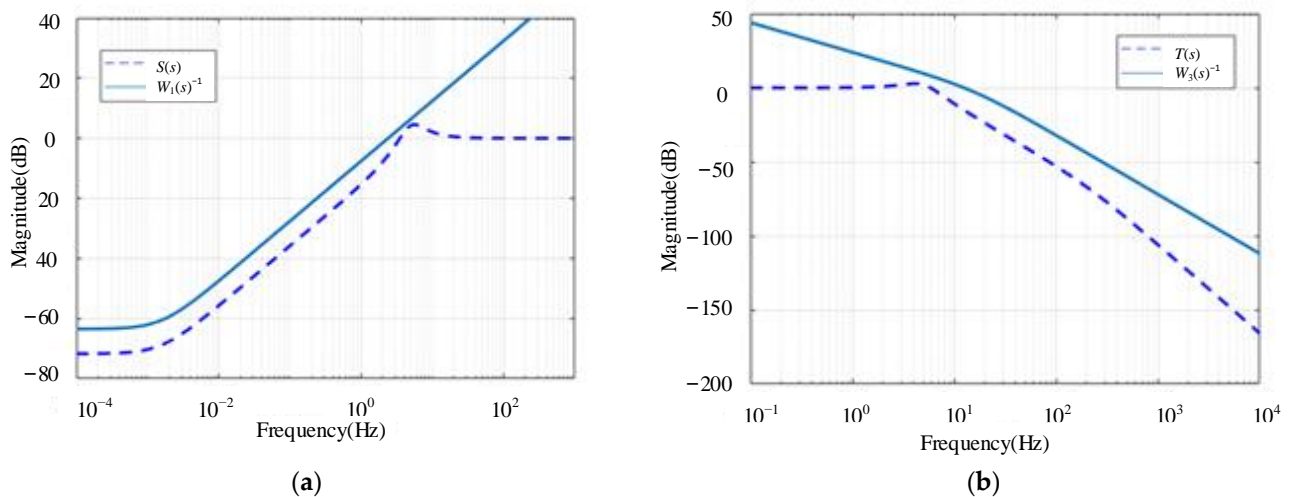


Figure 6. Amplitude–frequency curve. (a) Amplitude–frequency curve of $S(s)$ and $W_1^{-1}(s)$; (b) Amplitude–frequency curve of $T(s)$ and $W_3^{-1}(s)$.

4.1.2. Analysis of the Performance of the X Direction Control System

The amplitude-frequency characteristic curves of $S(s)$ and $W_1^{-1}(s)$ in the X direction are shown in Figure 7a. The amplitude of $\bar{\sigma}(S(s))$ is extremely small in the low-frequency range, and its maximum amplitude is less than $\bar{\sigma}(W_1^{-1}(s))$ in the whole frequency range, which satisfies Formula (20). Therefore, the anti-interference ability and tracking characteristics of the system are ensured. The amplitude-frequency characteristic curves of $T(s)$ and $W_3^{-1}(s)$ are shown in Figure 7b. $\bar{\sigma}(T(s))$ has a large slope in the high-frequency range, and

its maximum amplitude is smaller than $\bar{\sigma}(W_3^{-1}(s))$ in the whole frequency range, which satisfies Formula (21). It ensures that high-frequency noise is rapidly attenuated.

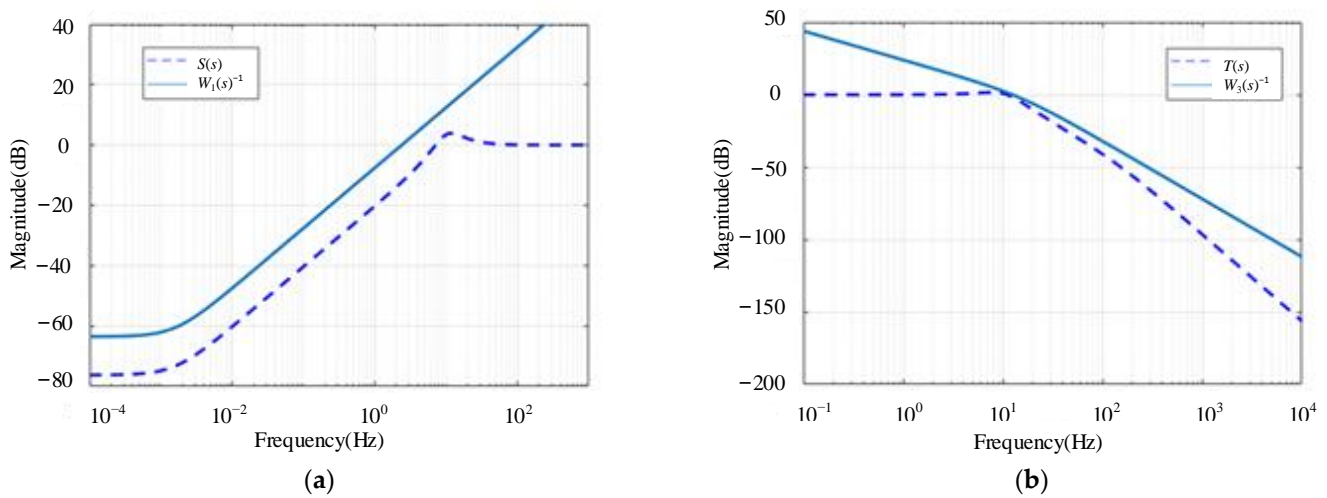


Figure 7. Amplitude–frequency curve. (a) Amplitude–frequency curve of $S(s)$ and $W_1^{-1}(s)$; (b) Amplitude–frequency curve of $T(s)$ and $W_3^{-1}(s)$.

4.1.3. Analysis of the Performance of the θ Direction Control System

The amplitude–frequency characteristic curves of $S(s)$ and $W_1^{-1}(s)$ in the θ direction are shown in Figure 8a. The amplitude of $\bar{\sigma}(S(s))$ is extremely small in the low-frequency range, and its maximum amplitude is less than $\bar{\sigma}(W_1^{-1}(s))$ in the whole frequency range, which satisfies Formula (20). Therefore, the anti-interference ability and tracking characteristics of the system are ensured. The amplitude–frequency characteristic curves of $T(s)$ and $W_3^{-1}(s)$ are shown in Figure 8b. $\bar{\sigma}(T(s))$ has a large slope in the high-frequency range, and its maximum amplitude is smaller than $\bar{\sigma}(W_3^{-1}(s))$ in the whole frequency range, which satisfies Formula (21). It ensures that high-frequency noise is rapidly attenuated.

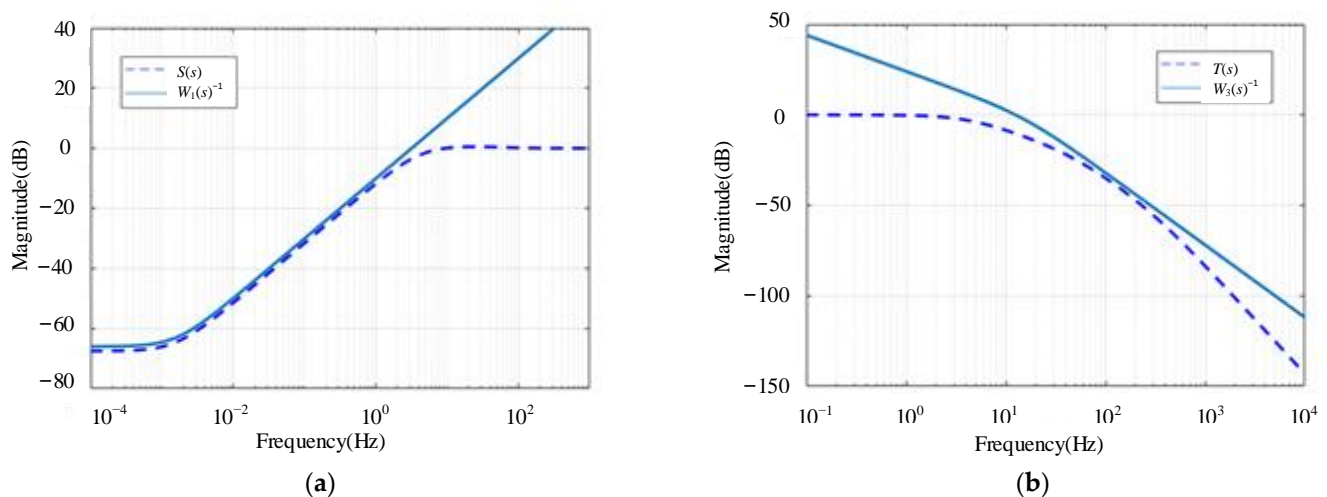


Figure 8. Amplitude–frequency curve. (a) Amplitude–frequency curve of $S(s)$ and $W_1^{-1}(s)$; (b) Amplitude–frequency curve of $T(s)$ and $W_3^{-1}(s)$.

4.2. Analysis of the System Response of the Standard Model

To verify the effect of the controller, MATLAB/Simulink is used to simulate and analyze the system.

The Y direction simulation: At 0.2 s, a signal of 0.1 mm is input in the Y direction. The system response results are shown in Figure 9a. The X direction simulation: At 0.2 s, a signal of 0.1 mm is input in the X direction. The system response results are shown in Figure 9b. The θ direction simulation: At 0.2 s, a signal of 0.1 mrad is input in the θ direction. The system response results are shown in Figure 9c.

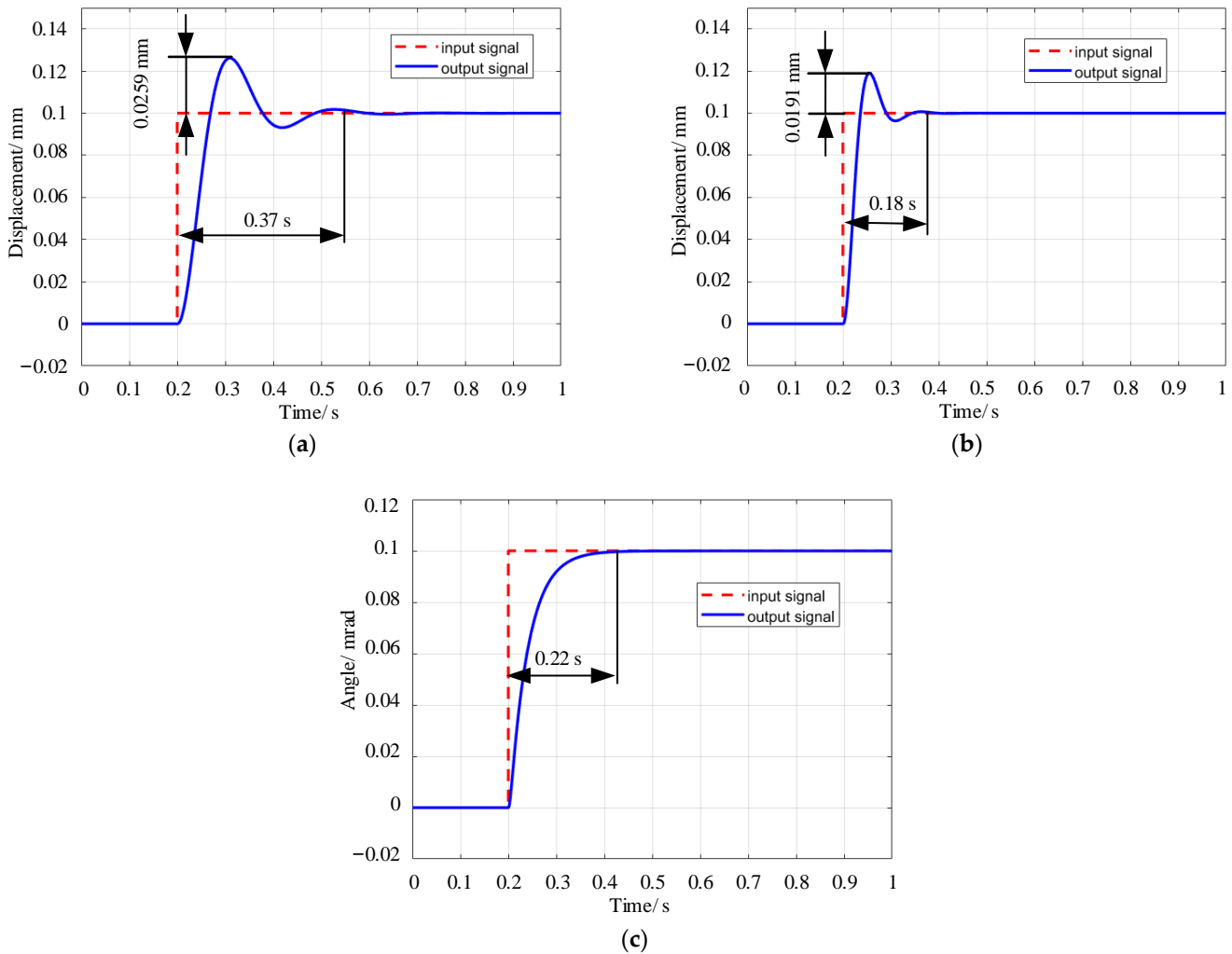


Figure 9. Step response. (a) Step response of Y direction; (b) Step response of X direction; (c) Step response of θ direction.

The performance indicators of the step response curve (Figure 9) in the Y, X, and θ directions are shown in Table 3.

Table 3. Performance index of each step response curve of the nominal model.

Direction	Maximum Overshoot	Regulation Time	Steady-State Error
Y direction	25.9%	0.37 s	0
X direction	19.1%	0.18 s	0
θ direction	0	0.22 s	0

According to the data in Table 3, the overshoot, adjustment time, and steady-state error in the Y direction are 25.9%, 0.37 s, and 0, respectively; in the X direction, they are 19.1%, 0.18 s, and 0; in the θ direction, they are 0, 0.22 s, and 0. Their steady-state performance meets the response requirements for laser off-axis cutting.

4.3. Analysis of System Response to Parameter Disturbance

The model of the system ignores some factors. A 20% perturbation of parameters is added to verify the system's robustness based on its standard model. Then, the parameters of the original controller were used to control the system, and its step response curve is shown in Figure 10.

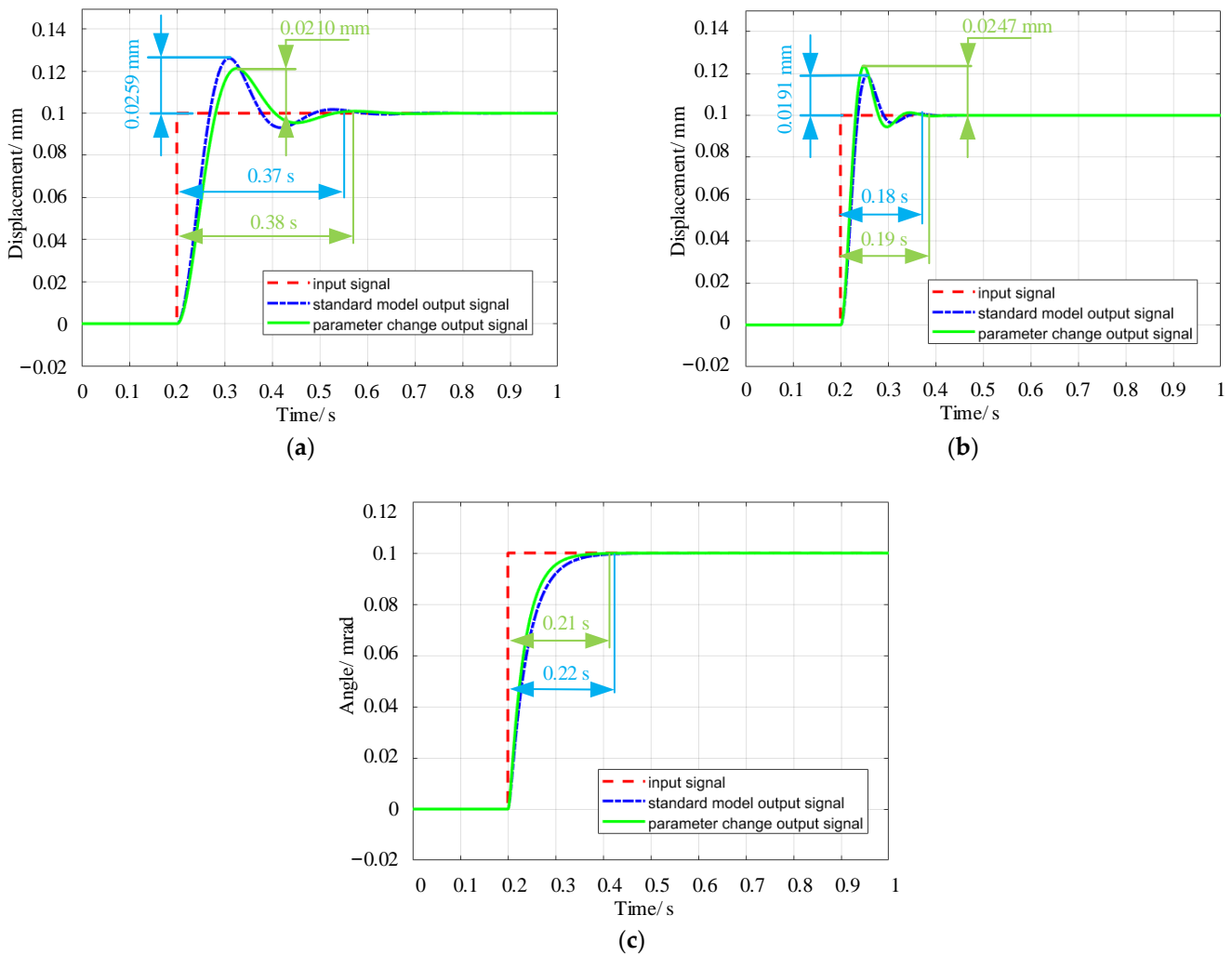


Figure 10. Step response. (a) Step response of Y direction with 20% parameters change; (b) Step response of X direction with 20% parameters change; (c) Step response of θ direction with 20% parameters change.

The performance indicators of the step response curve (Figure 10) in the Y, X, and θ directions are shown in Table 4.

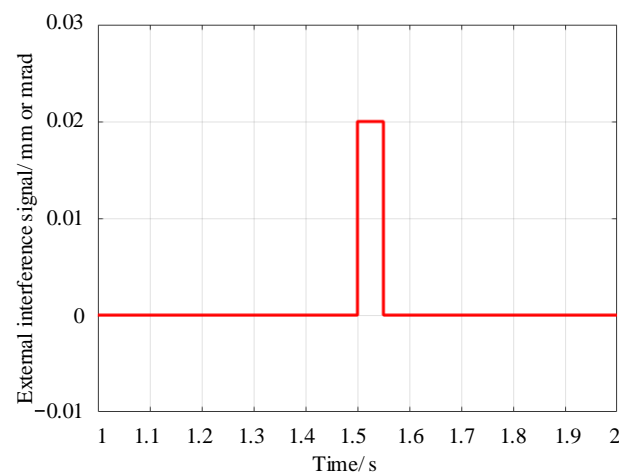
Table 4. Performance index of each step response curve of the model with parameter variation.

Direction	Maximum Overshoot	Regulation Time	Steady-State Error
Y direction	21%	0.38 s	0
X direction	24.7%	0.19 s	0
θ direction	0	0.21 s	0

The data in Table 4 show that after adding 20% parameter disturbance, the overshoot and adjustment time in the Y direction decrease from 25.9% to 21% and increase from 0.37 s to 0.38 s, respectively. The overshoot and adjustment time in the X direction increase from 19.1% to 24.7% and 0.18 s to 0.19 s, respectively. The θ direction adjustment time reduces from 0.22 s to 0.21 s. Steady-state errors are unchanged. In summary, compared with the standard model, the steady-state performance after adding 20% parameter disturbance has no significant change. It shows that the controller can still meet the performance requirements when the model is inaccurate.

4.4. Analysis of System Response to Impulse External Disturbance

An external pulse disturbance was input to verify the system's response in the case of external disturbances, and the results are shown in Figure 11. The vertical coordinates of Figure 11 have two units, "mm" and "mrad", respectively. The unit of vertical coordinate is "mm", which indicates the disturbance signal in Y and X directions. The unit of vertical coordinate is "mrad", which means the interference signal in θ direction.

**Figure 11.** Pulse interference signal.

After the external disturbance signal is input, the system can quickly recover to the steady-state value, and the steady-state error is 0, as shown in Figure 12.

The performance indicators of the step response curve (Figure 12) in the Y, X, and θ directions after being subjected to interference signals are shown in Table 5.

The data in Table 5 show that after adding the interference signal, the overshoot and adjustment time in the Y direction are 20% and 0.24 s, respectively. The overshoot and adjustment time in the X direction are 20% and 0.14 s, respectively. The overshoot and adjustment time in the θ direction are 20% and 0.16 s, respectively. The steady-state errors are unchanged. In summary, the steady-state performance after the interference signal has no significant change. It also indicates that the control method can effectively resist external interference.

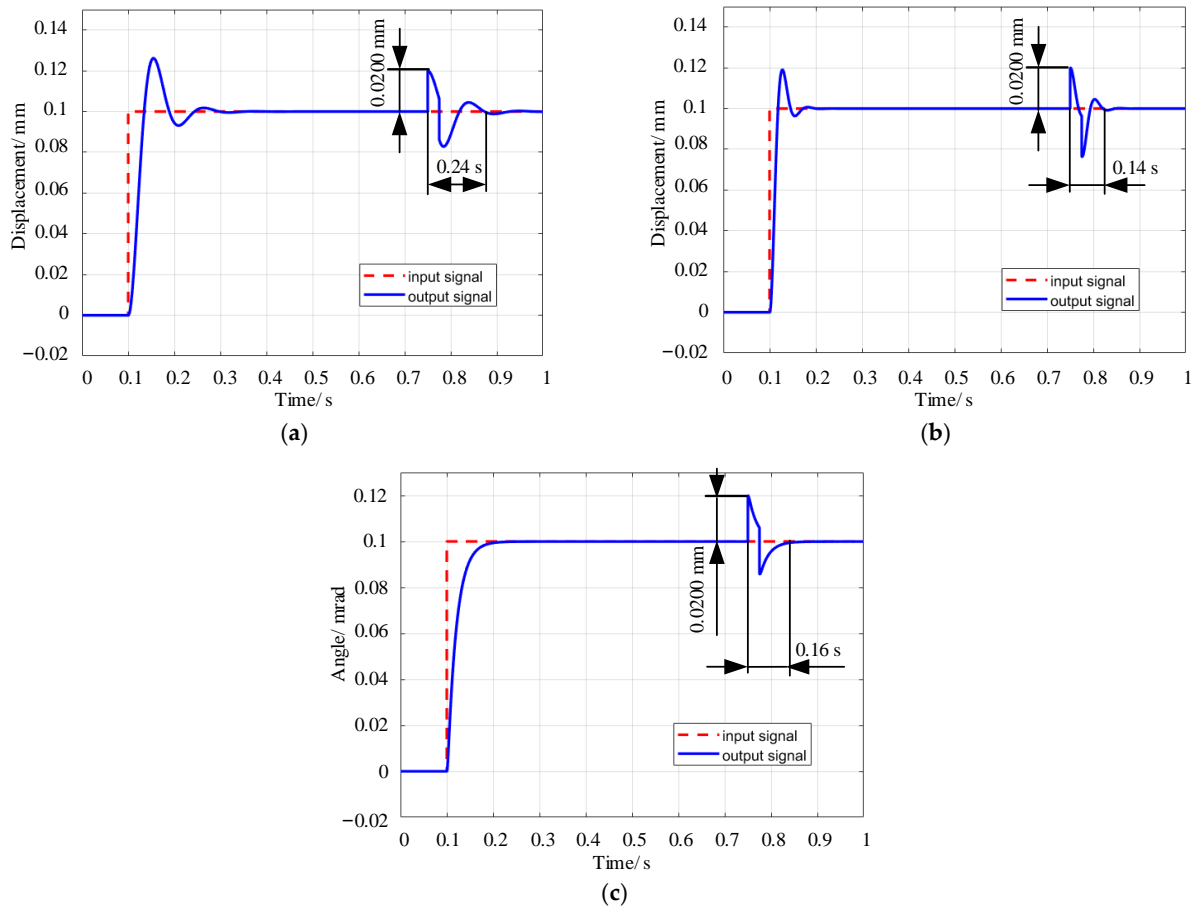


Figure 12. Step response. (a) Step response of Y direction with disturbance; (b) Step response of X direction with disturbance; (c) Step response of θ direction with disturbance.

Table 5. Performance index of each step response curve of the model with interference signal.

Direction	Maximum Overshoot	Regulation Time	Steady-State Error
Y direction	20%	0.24 s	0
X direction	20%	0.14 s	0
θ direction	20%	0.16 s	0

5. Experimental Verification

5.1. Experimental Equipment

Experiments were carried out to verify the controller's effectiveness in the laser focus position control. The experimental equipment mainly comprises a power amplifier (E120/06), eddy current sensor (EX-V10), dSPACE1104, actuator, etc., as shown in Figure 13. With dSPACE1104 as the core hardware, the mixed-sensitivity robust control of the actuator was performed to control its real-time position. We used dSPACE1104 to connect with MATLAB/Simulink for experiments seamlessly. First, the sensor detected the position signal and input it to the ADC module in dSPACE1104. After the control block diagram operation in Simulink, the input signal of the system was obtained. Second, the position signal detected by the sensor and the input signal of the system was subtracted to obtain the deviation signal. Then, the deviation signal was input into the controller in Simulink to obtain the control signal. Third, the control signal was input to the DAC module in dSPACE1104, and the input signal of the power amplifier was obtained. Finally, the power amplifier input the signal to three sets of differential electromagnets to realize real-time control of the actuator position.

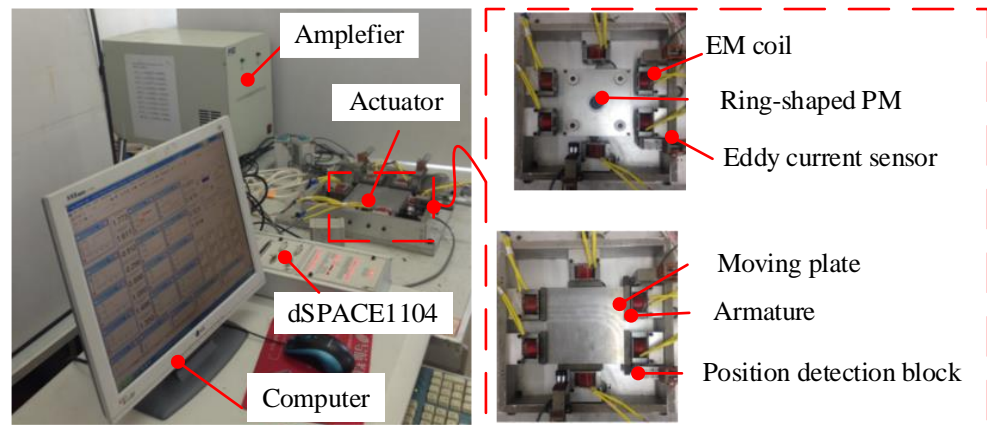


Figure 13. Experimental equipment. The equipment and actuator structures used in the experiments are shown.

5.2. Experimental Results

Step position control experiments were performed in the X and Y directions. First, an initial current of 1.2 A was fed to the three pairs of differential solenoids to make the actuator electromagnetically stiff in the X and Y directions. Then, the position compensation parameters of the system were adjusted so that the detection signal of the sensors was equal to the set value of the system.

When the system was stable, a step signal in the Y direction of 0.1 mm was input in 0.5 s, and the result is shown in Figure 14. The control current first increased and then leveled off. The system stabilized after 0.38 s with an overshoot of 0.034 mm. According to Figure 14, there was a time lag of 0.13 s, which was mainly caused by the following three reasons. First, in the actuator structure, there was only one pair of differential electromagnets in the Y direction and two pairs of differential electromagnets in the X direction, so the stiffness in the Y direction was smaller than that in the x direction. In the initial stage of current change, the driving force could not overcome the initial electromagnetic force. Second, the ring permanent magnet in the actuator was opposite the pole, so the attraction was larger, resulting in greater friction resistance. Third, to make the actuator in a wider range of stable control, the designed controller had robust conservatism. For these three reasons, the time lag was 0.13 s.

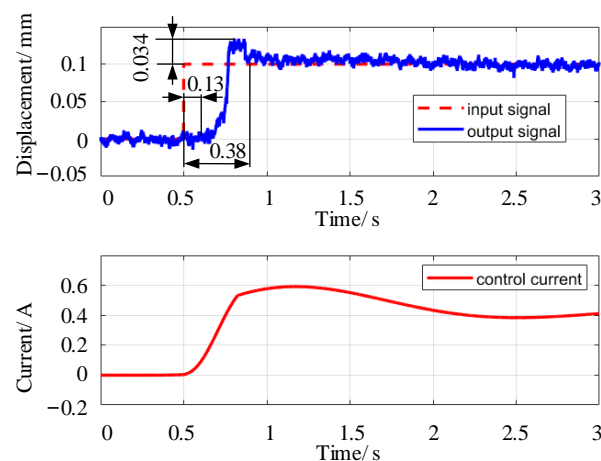


Figure 14. Step response of Y direction.

When the system is stable, we input 0.1 mm X direction step signal in 0.5 s, and the result is shown in Figure 15. According to Figure 15a, the control current of the system increases first and then becomes stable, reaching stability after 0.28 s. According to Figure 15b, after we input the X direction signal, 0.66 mrad fluctuation appears in the

direction of θ . This is because the motion of the actuator in both directions X and θ is driven by X direction 2 to the differential electromagnet, and there is coupling. According to Figure 15, control current 1 and control current 2 are not equal because there is an error in the actuator installation, which leads to the different initial air gaps between the two pairs of differential electromagnets in the X direction. Different initial air gaps will lead to different driving forces provided by two pairs of differential electromagnets in the X direction. After the actuator reaches equilibrium, the control current values will differ.

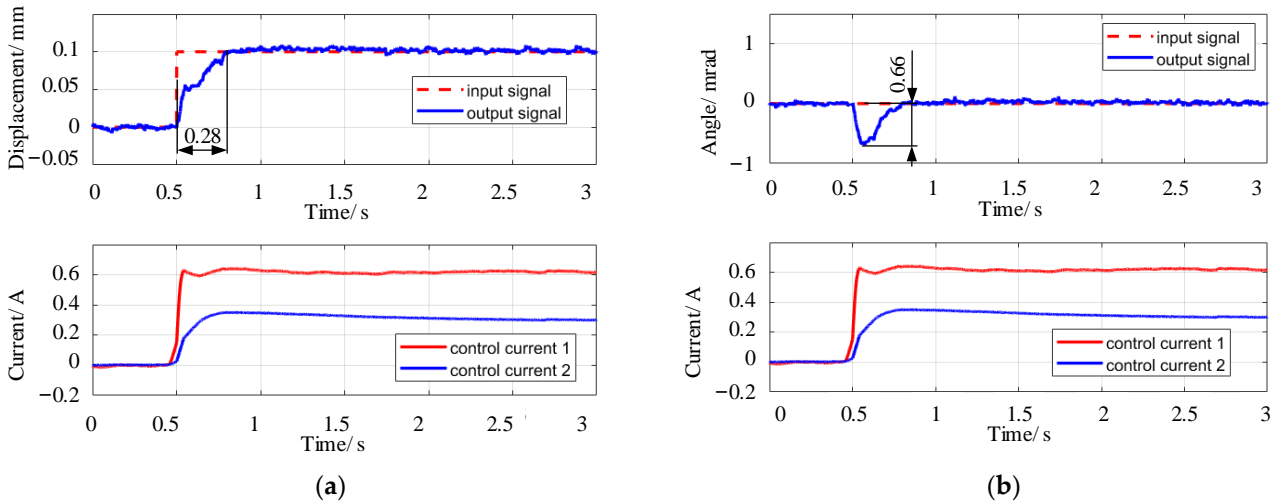


Figure 15. Step response of X direction. (a) The position and current signals in the X direction are shown; (b) The θ interfering position signal and current signal in the X direction are shown.

When the system is stable, a step signal in the direction of θ of 1.2 mrad is input in 0.5 s, and the result is shown in Figure 16. According to Figure 16a, control current 1 decreases first and then tends to be stable, while control current 2 increases first and then tends to be stable, and the output signal in the θ direction reaches the steady value in 0.29 s. According to Figure 16b, after we input θ signal, a fluctuation of 0.059 mm appears in the X direction. This is because the motion of the actuator in both X and θ directions is driven by X direction 2 to the differential electromagnet, and there is coupling.

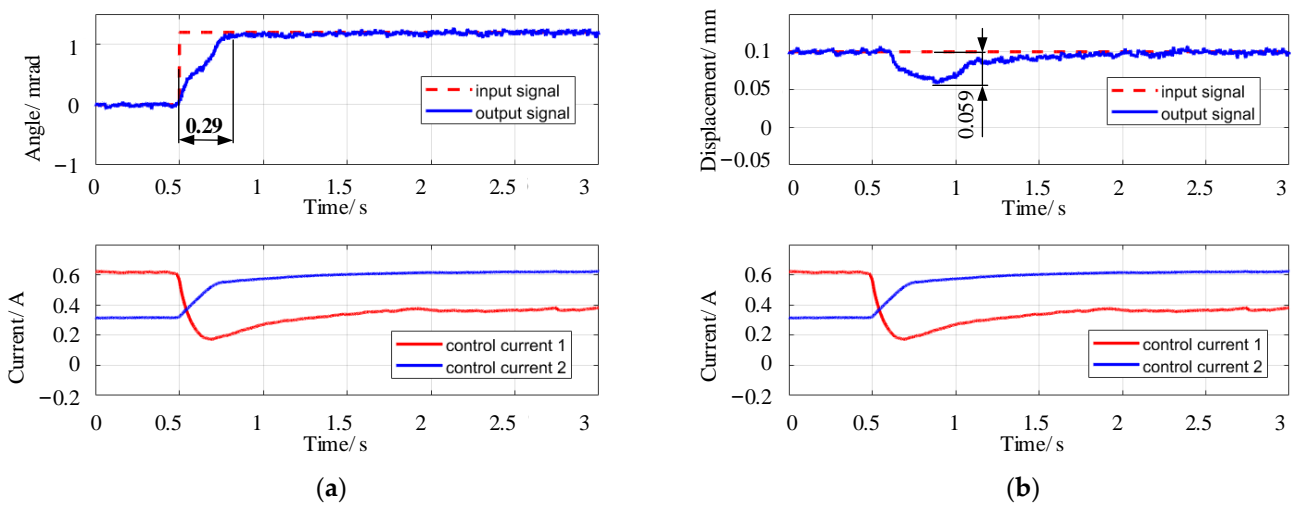


Figure 16. Step response. (a) The position and current signals in the θ direction are shown; (b) The X direction interfering position signal and current signal in the θ direction are shown.

The maximum overshoot in the Y direction is calculated as the maximum value between 0.5–1 s adjustment time, and the steady-state error is calculated as the average

value from 2–3 s. Since there is no obvious overshoot in the X direction and θ direction, the average value of 0.2 s after stabilization is taken as the maximum overshoot, and the steady-state error is taken as the average value of 2–3 s. The values are shown in Table 6.

Table 6. Performance index of the step response experiment in each direction.

Direction	Maximum Overshoot	Regulation Time	Steady-State Error
Y direction	34%	0.38 s	0.39%
X direction	3.1%	0.28 s	1.6%
θ direction	0%	0.29 s	0.45%

According to Table 6, the steady-state errors in the 3 directions are all less than 2.5%. That is, the system's error after stability can be made within 0.025 mm of the machine tool's accuracy in the position step response, which meets the performance requirements.

In order to be able to analyze the experimental data quantitatively. The simulated and experimental data are included in Table 7 for comparative analysis.

Table 7. Performance index of step response experiment in each direction.

Direction		Maximum Overshoot	Regulation Time	Steady-State Error
Y direction	Simulation	25.9%	0.37 s	0
	Experiment	34%	0.38 s	0.39%
	Difference value	8.1%	0.01 s	0.39%
X direction	Simulation	19.1%	0.18 s	0
	Experiment	3.1%	0.28 s	1.60%
	Difference value	16%	0.10 s	1.60%
θ direction	Simulation	0%	0.22 s	0
	Experiment	0%	0.29 s	0.45%
	Difference value	0%	0.07 s	0.45%

According to Table 7, the results of the standard model simulation are compared and analyzed with the experimental result data. The overshoot differences value in the Y, X, and θ directions are 8.1%, 16%, and 0%, respectively. The differences in adjustment time are 0.01 s, 0.10 s, and 0.07 s, respectively. The differences in steady-state errors are 0.39%, 1.60%, and 0.45%, respectively. The experimental and simulation data are slightly different because there are some non-artificial errors in the experiments, including the machining errors of the parts, assembly errors, etc. In addition, there is noise interference in the experiment, so it leads to some steady-state errors in the experiment.

6. Conclusions

A mixed sensitivity robust controller for a 3-DOF laser focal magnetic actuator is designed and simulated by MATLAB/Simulink. The following conclusions are obtained through simulation analysis and experimental verification.

1. The mixed sensitivity controller of the system is calculated by a reasonable selection of the weighting function, and the simulation analysis of the position step response in Y, X, and θ directions is carried out, and the steady-state errors are all 0. It shows that the designed controller has good position response characteristics.
2. Based on the standard model, 20% parameter variation is introduced, and the original controller simulates and analyzes the system. In the simulation of position step response in Y, X, and θ directions, the response characteristics are consistent with the results of the standard model. There are slight differences in overshoot and adjustment time between the above, and the steady-state error is 0. It shows that the system has better position response characteristics when the model is inaccurate.

3. When the external pulse disturbance is added to the system, the steady-state values of Y , X , and θ can be quickly restored in the position step experiment. It shows that the controller has good anti-interference properties.
4. There is a coupling phenomenon in the direction of X and θ , so both show certain coupling characteristics in the step response experiment. Still, the moving plate can be quickly adjusted to the steady-state value. The steady-state errors in the three directions are all less than 25%, which meets the requirement of machine tool accuracy of 0.025 mm.

In the future, we will optimize the structure of the actuator and design an actuator that can be mounted on the laser cutting head. Then, we will install it on the laser cutting machine for in-machine experimental research in order to explore the actuator's performance during the operation of the laser cutting head.

Author Contributions: Methodology, L.W.; validation, L.W. and Q.Z.; formal analysis, L.W.; resources, F.S.; data curation, L.W.; writing—original draft preparation, L.W.; writing—review and editing, L.T., G.Y., F.X., J.J., X.Z. and F.S. All authors have read and agreed to the published version of the manuscript.

Funding: This research is supported by National Natural Science Fund of China (No. 52005345, No. 52005344), National Key Research and Development Project (No. 2020YFC2006701), Scientific Research Fund Project of Liaoning Provincial Department of Education (No. LJKMZ20220506, No. LJKMZ20220460), Major Project of the Ministry of Science and Technology of Liaoning Province (No. 2022JH1/10400027).

Data Availability Statement: Not applicable.

Acknowledgments: We thank Zhou R., Zhao C., and Liu X. for their suggestions and recommendations.

Conflicts of Interest: The authors declare no conflict of interest.

Appendix A

$$\begin{aligned}
 F_e = & \left\{ 4\pi^2\mu_0 B_r n \delta_p \varepsilon (r_2^2 - r_1^2) [\pi r_2^2 (1 + \sqrt{\varepsilon^2 + e^2}) + 2(r_1 + r_2) \delta_p^2] [4\pi (r_2^2 - r_1^2) \varepsilon + 1.632(r_1 + r_2)(\varepsilon^2 + e^2)] \right\} 2 \\
 & \cdot e / \left\{ \left\{ \mu_r \pi (r_2^2 - r_1^2) \left\{ \delta_p (1 + \sqrt{\varepsilon^2 + e^2}) [4\pi (r_2^2 - r_1^2) \varepsilon + 1.632(r_1 + r_2)(\varepsilon^2 + e^2)] + (\varepsilon^2 + e^2) [\pi r_2^2 (1 + \sqrt{\varepsilon^2 + e^2}) \right. \right. \right. \\
 & \left. \left. \left. + 2(r_1 + r_2) \delta_p^2 \right\} \right\} + n \delta_p [\pi r_2^2 (1 + \sqrt{\varepsilon^2 + e^2}) + 2(r_1 + r_2) \delta_p^2] [4\pi (r_2^2 - r_1^2) \varepsilon + 1.632(r_1 + r_2)(\varepsilon^2 + e^2)] \right\} [4\pi \mu_0 (r_2^2 \\
 & - r_1^2) \varepsilon + 1.632 \mu_0 (r_1 + r_2)(\varepsilon^2 + e^2)] \right\}^2; \\
 e = & \sqrt{x^2 + y^2}
 \end{aligned} \tag{A1}$$

where ε is an axial air gap, e is radial displacement, t is the width of the ring permanent magnet, B_r is the remanence of permanent magnet material, n is the number of permanent magnets, δ_p is the thickness of permanent magnet, μ_r is the relative permeability of the magnetic ring, μ_0 is air permeability, r_1 is the inner radius of the annular permanent magnet, r_2 is the outer radius of the ring permanent magnet.

$$\begin{aligned}
 k_e = & 4\mu_0 \varepsilon^{-3} (r_2^2 - r_1^2) \left\{ B_r n \delta_p \pi (r_2^2 - r_1^2) [\pi r_2^2 (1 + \varepsilon) + 2(r_1 + r_2) \delta_p^2] [4\pi (r_2^2 - r_1^2) \varepsilon^{-1} + 1.632(r_1 + r_2)] \right\} 2 / \left\{ \left\{ \mu_r \pi (r_2^2 \right. \right. \\
 & - r_1^2) \left\{ \delta_p (1 + \varepsilon) [4\pi (r_2^2 - r_1^2) \varepsilon^{-1} + 1.632(r_1 + r_2)] + [\pi r_2^2 (1 + \varepsilon) + 2(r_1 + r_2) \delta_p^2] \right\} + n \delta_p [\pi r_2^2 (1 + \varepsilon) + 2(r_1 + r_2) \delta_p^2] \right. \\
 & \left. \left. [4\pi (r_2^2 - r_1^2) \varepsilon^{-1} + 1.632(r_1 + r_2)] \right\} [4\pi \mu_0 (r_2^2 - r_1^2) \varepsilon^{-1} + 1.632 \mu_0 (r_1 + r_2)] \right\}^2
 \end{aligned} \tag{A2}$$

References

1. He, Y.; Xie, H.; Ge, Y.; Lin, Y.; Yao, Z.; Wang, B.; Jin, M.; Liu, J.; Chen, X.; Sun, Y. Laser Cutting Technologies and Corresponding Pollution Control Strategy. *Processes* **2022**, *10*, 732. [\[CrossRef\]](#)
2. Singh, Y.; Singh, J.; Sharma, S.; Sharma, A.; Chohan, J. Process parameter optimization in laser cutting of Coir fiber reinforced Epoxy composite—A review. *Mater. Today Proc.* **2021**, *48*, 1021–1027. [\[CrossRef\]](#)
3. Sim, M.; Lee, C. Determination of optimal laser power according to the tool path inclination angle of a titanium alloy workpiece in laser-assisted machining. *Int. J. Adv. Manuf. Technol.* **2016**, *83*, 1717–1724. [\[CrossRef\]](#)

4. Jain, A.; Agarwal, A.; Chauhan, P.S. Optimization of laser cutting quality characteristics for basalt–glass hybrid composite using hybrid approach. *Mater. Today Proc.* **2022**, *62*, 12. [[CrossRef](#)]
5. Wang, H.; Yang, T. A review on laser drilling and cutting of silicon. *J. Eur. Ceram. Soc.* **2021**, *41*, 4997–5015. [[CrossRef](#)]
6. Marimuthu, S.; Dunleavey, J.; Liu, Y.; Antar, M.; Smith, B. Laser cutting of aluminium-alumina metal matrix composite. *Opt. Laser Technol.* **2019**, *117*, 251–259. [[CrossRef](#)]
7. Sharifi, M.; Akbari, M. Experimental investigation of the effect of process parameters on cutting region temperature and cutting edge quality in laser cutting of AL6061T6 alloy. *Optik* **2019**, *184*, 457–463. [[CrossRef](#)]
8. Mushtaq, R.T.; Wang, Y.; Rehman, M.; Khan, A.M.; Mia, M. State-Of-The-Art and Trends in CO2 Laser Cutting of Polymeric Materials—A Review. *Materials* **2020**, *13*, 3839. [[CrossRef](#)]
9. Li, M.; Han, H.; Jiang, X.; Zhang, X.; Chen, Y. Surface morphology and defect characterization during high-power fiber laser cutting of SiC particles reinforced aluminum metal matrix composite. *Opt. Laser Technol.* **2022**, *155*, 108419. [[CrossRef](#)]
10. Li, M.; Li, S.; Yang, X.; Zhang, Y.; Liang, Z. Effect of lay-up configuration and processing parameters on surface quality during fiber laser cutting of CFRP laminates. *Int. J. Adv. Manuf. Technol.* **2019**, *100*, 623–635. [[CrossRef](#)]
11. Elsheikh, A.; Deng, W.; Showaib, E. Improving laser cutting quality of polymethylmethacrylate sheet: Experimental investigation and optimization. *J. Mater. Res. Technol.* **2020**, *9*, 1325–1339. [[CrossRef](#)]
12. Vora, J.; Chaudhari, R.; Patel, C.; Pimenov, D.; Patel, V.; Giasin, K.; Sharma, S. Experimental investigations and Pareto optimization of fiber laser cutting process of Ti6Al4V. *Metals* **2021**, *11*, 1461. [[CrossRef](#)]
13. Hong, L.; Zhang, Y.; Mi, C. Technological study of laser cutting silicon steel controlled by rotating gas flow. *Opt. Laser Technol.* **2009**, *41*, 328–333. [[CrossRef](#)]
14. Quintero, F.; Pou, J.; Fernandez, J.L.; Doval, A.F.; Lusquiños, F.; Boutinguiza, M.; Soto, R.; Pérez-Amor, M. Optimization of an off-axis nozzle for assist gas injection in laser fusion cutting. *Opt. Lasers Eng.* **2006**, *44*, 1158–1171. [[CrossRef](#)]
15. Riveiro, A.; Quintero, F.; Boutinguiza, M.; Del Val, J.; Comesaña, R.; Lusquiños, F.; Pou, J. Laser cutting: A review on the influence of assist gas. *Materials* **2019**, *12*, 157. [[CrossRef](#)]
16. Riveiro, A.; Quintero, F.; Lusquiños, F.; Comesaña, R.; Pou, J. Effects of processing parameters on laser cutting of aluminium-copper alloys using off-axial supersonic nozzles. *Appl. Surf. Sci.* **2011**, *257*, 5393–5397. [[CrossRef](#)]
17. Riveiro, A.; Quintero, F.; del Val, J.; Boutinguiza, M.; Comesaña, R.; Lusquiños, F.; Pou, J. Laser cutting using off-axial supersonic rectangular nozzles. *Precis. Eng.* **2018**, *51*, 78–87. [[CrossRef](#)]
18. Yagi, A.; Kadonaga, S.; Okamoto, Y.; Ishiguro, H.; Ito, R.; Sugiyama, A.; Okawa, H.; Fujita, R.; Okada, A. Fundamental study on reduction of dross in fiber laser cutting of steel by shifting nozzle axis. *J. Laser Appl.* **2021**, *33*, 012022. [[CrossRef](#)]
19. Murakami, I.; Zhao, Y.; Tashiro, T. Stabilization of a Magnetic Repulsive Levitation Flywheel System Using a High-Efficiency Superconducting Magnetic Bearing. *Actuators* **2022**, *11*, 180. [[CrossRef](#)]
20. Soni, T.; Dutt, J.; Das, A.S. Parametric stability analysis of active magnetic bearing supported rotor system with a novel control law subject to periodic base motion. *IEEE Trans. Ind. Electron.* **2019**, *67*, 1160–1170. [[CrossRef](#)]
21. Sillanpää, T.; Smirnov, A.; Jaatinen, P.; Vuojolainen, J.; Nevaranta, N.; Jastrzebski, R.; Pyrhönen, O. Three-axis inductive displacement sensor using phase-sensitive digital signal processing for industrial magnetic bearing applications. *Actuators* **2021**, *10*, 115. [[CrossRef](#)]
22. Cao, S.; Niu, P.; Wang, W.; Zhao, T.; Liu, Q.; Bai, J.; Sheng, S. Novel Magnetic Suspension Platform with Three Types of Magnetic Bearings for Mass Transfer. *Energies* **2022**, *15*, 5691. [[CrossRef](#)]
23. Javed, A.; Mizuno, T.; Takasaki, M.; Ishino, Y.; Hara, M.; Yamaguchi, D. Lateral Vibration Suppression by Varying Stiffness Control in a Vertically Active Magnetic Suspension System. *Actuators* **2018**, *7*, 21. [[CrossRef](#)]
24. Ren, G.P.; Chen, Z.; Zhang, H.; Wu, Y.; Meng, H.; Wu, D.; Ding, H. Design of interval type-2 fuzzy controllers for active magnetic bearing systems. *IEEE/ASME Trans. Mechatron.* **2020**, *25*, 2449–2459. [[CrossRef](#)]
25. Fan, X.; Yin, J.; Lu, Q. Design and Analysis of a Novel Compositated Electromagnetic Linear Actuator. *Actuators* **2022**, *11*, 6. [[CrossRef](#)]
26. Xu, Y.; Jiang, Q.; Yang, K.; Zhou, J.; Guo, Q. A novel ultra-high-resolution inclination sensor based on diamagnetic levitation. *Sens. Actuators A Phys.* **2022**, *343*, 113686. [[CrossRef](#)]
27. Zhang, X.; Shinshi, T.; Fukuoka, T.; Nakai, T. Development of a 2-DOF Controlled Magnetic Drive Actuator for Laser Beam Cutting. *J. Adv. Mech. Des. Syst. Manuf.* **2013**, *7*, 448–457. [[CrossRef](#)]
28. He, D.; Shinshi, T.; Nakai, T. Development of a maglev lens driving actuator for off-axis control and adjustment of the focal point in laser beam machining. *Precis. Eng.* **2013**, *37*, 255–264. [[CrossRef](#)]
29. He, D.; Shinshi, T.; Nakai, T. Development of a Lens Driving Maglev Actuator for Laser Beam Off-Axis Cutting and Deep Piercing. In *Key Engineering Materials*; Trans Tech Publications Ltd.: Bäch, Switzerland, 2012; Volume 523, pp. 774–779. [[CrossRef](#)]
30. Morimoto, Y.; Shinshi, T.; Nakai, T. A two-DOF controlled lens drive actuator for off-axis laser beam cutting. *J. Adv. Mech. Des. Syst. Manuf.* **2012**, *6*, 875–884. [[CrossRef](#)]
31. Gasmí, N.; Boutayeb, M.; Thabet, A.; Bel Haj Frej, G.; Aoun, M. Robust Control of a Class of Nonlinear Discrete-Time Systems: Design and Experimental Results on a Real-Time Emulator. *Actuators* **2021**, *10*, 303. [[CrossRef](#)]
32. Seyfi, N.; Khalaji, A. Robust control of a cable-driven rehabilitation robot for lower and upper limbs. *ISA Trans.* **2022**, *125*, 268–289. [[CrossRef](#)] [[PubMed](#)]

33. Zhang, X.; Ma, K.; Wei, Y.; Han, Y. Finite-time robust H_∞ control for high-speed underwater vehicles subject to parametric uncertainties and disturbances. *J. Mar. Sci. Technol.* **2017**, *22*, 201–218. [[CrossRef](#)]
34. Bu, X.; Wu, X.; Wei, D.; Huang, J. Neural-approximation-based robust adaptive control of flexible air-breathing hypersonic vehicles with parametric uncertainties and control input constraints. *Inf. Sci.* **2016**, *346*, 29–43. [[CrossRef](#)]
35. Gosiewski, Z.; Mystkowski, A. Robust control of active magnetic suspension: Analytical and experimental results. *Mech. Syst. Signal Process.* **2008**, *22*, 1297–1303. [[CrossRef](#)]
36. Zhang, Q.; Yu, R.; Li, C.; Chen, Y.-H.; Gu, J. Servo Robust Control of Uncertain Mechanical Systems: Application in a Compressor/PMSM System. *Actuators* **2022**, *11*, 42. [[CrossRef](#)]
37. Zhang, K.; Scorletti, G.; Ichchou, M.; Mieleveville, F. Quantitative robust linear parameter varying H_∞ vibration control of flexible structures for saving the control energy. *J. Intell. Mater. Syst. Struct.* **2015**, *26*, 1006–1027. [[CrossRef](#)]
38. Ko, Y.; Kim, T. Feedforward Plus Feedback Control of an Electro-Hydraulic Valve System Using a Proportional Control Valve. *Actuators* **2020**, *9*, 45. [[CrossRef](#)]
39. Isbeih, Y.; El Moursi, M.; Xiao, W.; El-Saadany, E. H_∞ mixed-sensitivity robust control design for damping low-frequency oscillations with DFIG wind power generation. *IET Gener. Transm. Distrib.* **2019**, *13*, 4274–4286. [[CrossRef](#)]
40. Wu, X.; Xu, C.; Wei, B.; Xia, C.; Li, X. H_∞ mixed sensitivity robust control method of relay ICPT system for output voltage regulation. *Electr. Eng.* **2021**, *103*, 781–792. [[CrossRef](#)]
41. Xu, Z.; Zhang, Q.; Sun, F. Analysis of Wave Characteristics of Laser Focus Magnetic Drive Platform. *Modul. Mach. Tool Autom. Manuf. Tech.* **2020**, *3*, 13–15. [[CrossRef](#)]
42. Tian, L.; Ai, X.P.; Tian, Y. Analytical model of magnetic force for axial stack permanent-magnet bearings. *IEEE Trans. Magn.* **2012**, *48*, 2592–2599. [[CrossRef](#)]

Disclaimer/Publisher’s Note: The statements, opinions and data contained in all publications are solely those of the individual author(s) and contributor(s) and not of MDPI and/or the editor(s). MDPI and/or the editor(s) disclaim responsibility for any injury to people or property resulting from any ideas, methods, instructions or products referred to in the content.